Volume 7
Number 9
September 2020
Pages 2173–2464

Materials Horizons

rsc.li/materials-horizons

ISSN 2051-6347

ROYAL SOCIETY OF CHEMISTRY

COMMUNICATION
Anna C. Balazs *et al.*
Chemically controlled shape-morphing of elastic sheets

Materials Horizons

ROYAL SOCIETY OF CHEMISTRY

COMMUNICATION

View Article Online
View Journal | View Issue

Cite this: *Mater. Horiz.*, 2020, 7, 2314

Received 1st May 2020,
Accepted 12th June 2020

DOI: 10.1039/d0mh00730g

rsc.li/materials-horizons

Chemically controlled shape-morphing of elastic sheets†

Raj Kumar Manna, [a] Oleg E. Shklyaev,[a] Howard A. Stone[b] and Anna C. Balazs *[a]

Two-dimensional responsive materials that change shape into complex three-dimensional structures are valuable for creating systems ranging from wearable electronics to soft robotics. Typically, the final 3D structure is unique and predetermined through the materials' processing. Here, we use theory and simulation to devise a distinctive approach for driving shape changes of 2D elastic sheets in fluid-filled microchambers. The sheets are coated with catalyst to generate controllable fluid flows, which transform the sheets into complex 3D shapes. A given shape can be achieved by patterning the arrangement of the catalytic domains on the sheet and introducing the appropriate reactant to initiate a specific catalytic reaction. Moreover, a single sheet that encompasses multiple catalytic domains can be transformed into a variety of 3D shapes through the addition of one or more reactants. Materials systems that morph on-demand into a variety of distinct structures can simplify manufacturing processes and broaden the utility of soft materials.

New concepts

Using theory and simulation, we designed a catalyst-coated 2D sheet that controllably morphs into multiple 3D structures in fluid-filled microchambers. The advent of materials where a single sample morphs on-demand into various 3D shapes can dramatically simplify manufacturing processes and enable the creation of stand-alone, multifunctional soft robots. Currently, shape-morphing 2D structures encompass non-uniform internal stresses that yield a specific 3D form with the application of external stimuli. This final 3D configuration is unique and predetermined through the materials' processing. Here, we harness the inherent chemo-mechanical transduction that occurs when a reactant initiates a catalytic reaction in solution. The resultant chemical energy is transduced into the flow of the surrounding fluid. In turn, the forces from the flow "sculpt" the flexible sheet into the 3D shapes. We also exploit the fact that catalytic reactions can only be initiated by specific reactants. Hence, for a sheet encompassing multiple catalytic patches, the 3D shape can be controlled through the addition of a particular reactant or combination of reactants, enabling one sheet to form multiple architectures. Our models provide new insights into the relationships among catalytic reactions, patterns on the sheet, and generated flows, providing guidelines for driving novel 2D-to-3D shape transformations.

Introduction

The shape-morphing of two-dimensional elastic materials into three-dimensional structures is a vital and ubiquitous transformation in biological systems,[1–3] as evidenced, for example, by the morphogenesis in cells and tissues,[4] the formation of well-defined curvatures in growing flowers and leaves,[5] and reconfiguration of seedpods in the release of seeds.[1] The functionality of such biological reconfigurations has inspired the development of synthetic shape-changing materials that are useful for soft robotics,[6–8] biomedical devices,[9,10] soft actuators,[11] and bio-inspired engineering.[12,13] Typically, shape-morphing structures are created by introducing non-uniform internal stresses within layers of soft, compliant materials, such as shape memory polymers,[14,15] stimuli-responsive hydrogels,[16–19] and liquid-crystalline elastomers.[20,21] The inhomogeneous stresses can be generated by joining 2D materials with different mechanical properties,[22,23] or incorporating gradients[16,24,25] and spatially varying micropatterns within the layers.[18,26,27] Once these stress patterns have been inscribed into the material, the 2D structures can morph into 3D forms with the application of external stimuli (such as light, pressure, temperature, electromagnetic fields, absorbed fluids[28–33]). The final 3D configuration, however, is completely predetermined by the pattern of built-in stresses or material characteristics. Here, we use computational modeling[34,35] to design self-contained systems where a single catalyst-coated 2D sheet in solution generates the fluid flows that, in turn, controllably transform one sheet into multiple 3D structures. The advent of materials systems where a single sample can morph on-demand into a variety of

[a] *Department of Chemical Engineering, University of Pittsburgh, Pittsburgh, PA 15260, USA. E-mail: balazs@pitt.edu*
[b] *Department of Mechanical and Aerospace Engineering, Princeton University, Princeton, New Jersey 08544, USA*

† Electronic supplementary information (ESI) available. See DOI: 10.1039/d0mh00730g

distinct shapes has the potential to dramatically simplify manufacturing processes and broaden the utility and applicability of soft materials.

In devising these mutable materials, we focus on compliant sheets that are coated with patches of different catalysts and immersed in a fluid-filled microchamber. We take advantage of the chemo-mechanical transduction that converts the energy of the catalytic reaction into the motion of the confined fluid.[36,37] We also exploit the specificity of catalytic reactions: the catalysis is only activated in the presence of certain reactants. In effect, the appropriate reactants (and products) serve as inherent chemical stimuli that enable the structural transformation. For example, depending on the chemical stimuli, the same enzyme-coated sheet can morph into either a dome-like or bowl-like or rolled shaped structure (as detailed below). The set of 3D shapes that are formed can be altered by the varying the elastic properties of the sheet, and the shape and position of the different catalytic patches on the sheet. To complement these computational studies, we develop a lubrication model capable of capturing the initial dynamic behavior of the elastic sheet. Notably, when the ratio of the thickness of the fluidic domain to its length is sufficiently small, the lubrication model shows quantitative agreement with the key phenomena observed in the simulations.

Such chemically-driven shape-morphing structures can facilitate the development of "multi-tasking" soft robots that operate in a self-sustained manner in fluidic environments. Since a single sheet can be fashioned into different forms, the soft robot could perform a range of tasks, without the need for extensive extraneous control, or thermal and electric input.[36,37] Moreover, these sheets can act as effective chemical sensors: the morphing of the sheet into a specific structure can reveal the presence of a particular chemical in the solution. Additionally, a single sheet coated with multiple enzymatic patches could be used to perform several assays simultaneously in microfluidic devices.

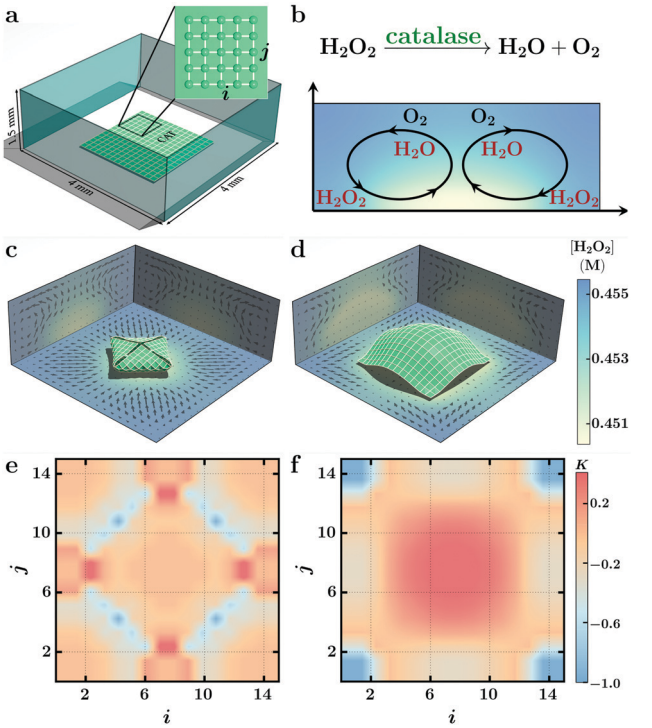

Fig. 1 Shape-morphing of an active sheet. (a) Schematic view of a fluid chamber containing an enzyme-coated elastic sheet. The zoom-in shows a network of nodes (marked by green dots) in the elastic sheet and the flexible bonds between nodes (white lines). (b) Each node decomposes reactant into products. For example, a catalase-coated sheet decomposes hydrogen peroxide (H_2O_2) into the less dense products water (H_2O) and oxygen (O_2), which rise upward to produce inward convective flow at the bottom of the chamber. (c and d) Self-folding of the catalase-coated sheet into an envelope-like (c) structure for bending modulus of the sheet κ_b = 0.40 pN mm^2. For larger bending modulus (κ_b = 0.49 pN mm^2), the sheet morphs into a dome-like structure (d) (see Movie S1, ESI†). Black arrows indicate the direction and magnitude of the fluid flow and the color bar indicates the concentration of H_2O_2 in the solution. Fluid flows at two vertical planes passing through the middle of the chamber are projected onto two vertical walls of the chamber. The configurations of the elastic sheet in (c and d) are respectively at 390 and 320 minutes after the start of the catalytic reaction. The stretching modulus of the sheet is taken as κ_s = 20 pN. The reaction rate is $r_{m,\text{sheet}}^{\text{catalase}}$ = 5.2 × 10^{-6} mol m^{-2} s^{-1}. (e and f) Plots for the corresponding Gaussian curvature, K, for the sheet configurations in (c) and (d). Here, (i,j) denotes the position of the node. The color bar indicates the Gaussian curvature normalized by its maximum magnitude.

Results

Theoretical modelling of chemically active sheets

We consider a fluid-filled microchamber that contains an enzyme-coated elastic sheet (Fig. 1a). The elastic sheet is modeled as a planar network of N chemically active nodes, with positions $\mathbf{r}_k$ $(1 \le k \le N)$, that are interconnected by elastic rods shown in white in the inset of Fig. 1a. The enzymatic reactions on the surface of the sheet are coupled to the motion of the surrounding fluid through a solutal buoyancy mechanism. Namely, the enzymes decompose the chemical reactants into products, which can occupy different volumes than the reactants and thus alter the local density of the fluid. In response to the spatial distribution of chemicals, the fluid density can be approximated as $\rho = \rho_0(1 + \sum \beta_i C_i)$, where ρ_0 is the solvent density, C_i is the concentration of chemical species i and $\beta_i = \frac{1}{\rho_0}\frac{\partial \rho}{\partial C_i}$ are the corresponding solutal expansion coefficients. Since the temperature changes due to the chemical reactions considered here are small and the thermal expansion coefficients are significantly smaller than the solutal expansion coefficients, we treat the systems as isothermal. We also neglect any enthalpic changes associated with the mixing of the chemical species.

The density variation in the solution gives rise to a buoyancy force per unit volume that is given by $\mathbf{F}_b = \mathbf{g}\rho_0 \sum \beta_i C_i$, where $\mathbf{g}$ is gravitational acceleration. This buoyancy force density drives the spontaneous motion of the fluid. If the products of the reactions are less dense than the reactants, the product-rich fluid flows upward and the reactant-rich fluid flows along the surface toward the patch. This motion is referred to as "inward" flow. Alternatively, if the products are denser than the reactants, then the product-rich fluid flows along the surface and away from the patch to produce an "outward" flow.

The generated fluid flow in turn drags the constituent nodes of the elastic sheet, and thus, affects the configurations of this layer. As a result, the nodes forming the sheet experience elastic forces $\mathbf{F}_{el}$, which resist the stretching and bending of bonds connecting the nodes. The elastic forces are characterized by the stretching (κ_s) and bending (κ_b) moduli and are governed by the linear constitutive relations for a Kirchoff rod[38] (see Methods). The excluded volume of the sheet is modeled through a ''node-node'' (nn) steric repulsion between two nodes l and k as $\mathbf{F}^{nn}(\mathbf{r}_l - \mathbf{r}_k) = -\dfrac{\partial U(r)}{\partial \mathbf{r}}$, where $U(r)$ is the Morse potential:

$$U(r) = \begin{cases} \varepsilon(1 - \exp[-\omega(r - r_0)])^2, & r < r_0 \\ 0, & r \geq r_0 \end{cases} \quad (1)$$

Here, $r = |\mathbf{r}_l - \mathbf{r}_k|$ is the distance between nodes, ε and ω are the respective strength and the width of the potential, and r_0 is the equilibrium distance characterizing the potential. The steric repulsion between nodes and any of the six confining walls (denoted nw) is described by $\mathbf{F}^{nw}\left(\mathbf{r}_k - \mathbf{r}_k^{W_j}\right)$, where $\mathbf{r}_k - \mathbf{r}_k^{W_j}$ denotes the vector between node k and closest point on the wall W_j ($1 \leq j \leq 6$). $\mathbf{F}^{nw}(r) = -\dfrac{\partial U(r)}{\partial \mathbf{r}}$ is computed using the same functional form of the potential given in eqn (1).

We assume that the density of the sheet (ρ_s) is greater than the density of the solvent (ρ_0). Therefore, all the nodes in the sheet experience a gravitational force $\mathbf{F}_g = V(\rho_s - \rho_0)\mathbf{g}$, where V is the effective volume of each node, defined by the volume of the sheet divided by the total number of nodes in the sheet. The gravitational force drives the sedimentation of the sheet to the bottom of the chamber where this force is countered by the excluded volume interaction ($\mathbf{F}^{nw}$) between the sheet nodes and the wall. With the chosen form of the repulsion potential (eqn (1)), we tuned parameters ε and ω to ensure that the equilibrium distance between a sheet node and the wall is approximately equal to r_0.

The coupled, governing equations that describe the dynamic interactions between the elastic sheet and the flowing fluid are: the continuity and Navier–Stokes (in the Boussinesq approximation[39]) equations for the dynamics of an incompressible flow; the equation for the advection, diffusion and reaction of the dissolved chemical species C_i; and the equation for the body force density acting on the fluid. The respective equations are

$$\nabla \cdot \mathbf{u} = 0, \quad (2)$$

$$\frac{\partial \mathbf{u}}{\partial t} + (\mathbf{u} \cdot \nabla)\mathbf{u} = -\frac{1}{\rho_0}\nabla p + \nu \nabla^2 \mathbf{u} + \frac{1}{\rho_0}\mathbf{F}, \quad (3)$$

where $F = \underbrace{\mathbf{g}\rho_0 \sum \beta_i C_i}_{\text{solutal buoyancy}} + \underbrace{(\rho_s - \rho_0)\mathbf{g} + \frac{1}{V}\left(\mathbf{F}_{el} + \sum \mathbf{F}^{nw} + \sum \mathbf{F}^{nn}\right)}_{\text{sheet}}$,

$$\frac{\partial C_i}{\partial t} + (\mathbf{u} \cdot \nabla)C_i = D_i \nabla^2 C_i \pm S K_d \sum_{k=1}^{N_a} \delta(\mathbf{r}_k - \mathbf{r}), \quad (4)$$

$$\frac{\partial \mathbf{r}_k}{\partial t} = \mathbf{u}. \quad (5)$$

Here, $\mathbf{u}$ and p (in eqn (3)) are the local fluid velocity and pressure respectively, ν is the kinematic viscosity of the fluid, ∇ is the spatial gradient operator, and ρ_s is the density of the material forming the sheet. The body force density (force per unit volume) $\mathbf{F}$ is the sum of the buoyancy force density and the body force density applied to the fluid by the immersed elastic sheet. The immersed boundary method (IBM)[40] is used to treat the fluid-structure interactions between the solution and the elastic sheet (see Methods).

The i-th reagent of concentration C_i diffuses with the diffusion constant D_i. The chemical is consumed or produced at the position of catalytic node $\mathbf{r}_k$ of the sheet with a reaction rate given by SK_d where S is the surface area per node. The catalytic reactions are modeled using Michaelis–Menten reaction rates.[41] The Michaelis–Menten model is one of the most well-known and widely used models for enzyme kinetics, and hence we use this approach in our model. Thus, K_d the rate of reaction per unit area, is given as

$$K_d = \frac{r_{m,sheet}^{enzyme} C_i}{K_M + C_i} \quad (6)$$

Here, K_M (in units of molarity, M) is the Michaelis–Menten constant. The maximal reaction rate $r_{m,sheet}^{enzyme} = k_e[E]$ (in units of M m^{-2} s^{-1}) is described by the product of the reaction rate per molecule of enzyme k_e (s^{-1}) and the areal concentration of enzyme, [E] (M m^{-2}).

We use no-slip boundary conditions for the fluid flow ($\mathbf{u} = 0$) at the confining walls of the chamber. For the concentration of chemical C_i, we use two different boundary conditions at the solid walls: (i) no chemical penetration through the walls, and (ii) the walls are coated with enzyme and take part in the catalytic reactions. The respective boundary conditions at the solid walls, with surface normal $\hat{\mathbf{n}}$ pointing into the fluid domain, are specified as

$$-D_i \frac{\partial C_i}{\partial n} = \begin{cases} 0 & \text{(i) no-flux wall} \\ \dfrac{r_{m,wall}^{enzyme} C_i}{K_M + C_i} & \text{(ii) enzyme-coated wall} \end{cases} \quad (7)$$

The numerical methods for solving the governing equations (eqn (2)–(5)) with the specific boundary conditions (eqn (7)) are described in the Methods section and the parameters relevant to chemical reactions are provided in Tables 1 and 2.

The fluid velocities generated by the catalytic reactions at the surface of the sheet and the elastic parameters of the sheet determine the sheet's configuration *via* eqn (5). The speed of the fluid flow is controlled by the rate of chemical transformations, which depends on the per-node area of the enzyme-coated surface S, the magnitude of the reaction rate per molecule of enzyme (k_e), and areal concentration of the enzyme molecules [E]. The buoyancy force generated in a chamber of height H with initial concentration of chemical C_0 can be characterized by the Grashof number, $\dfrac{g\beta C_0 H^3}{\nu^2}$, which implies that the flow velocities can be increased by either using chemicals with higher expansion coefficients, increasing the

Table 1 Physical properties of chemicals

Chemicals	Density ρ (g cc^{-1})	Diffusivity D m^2 s^{-1}	Molar mass m_m (g mol^{-1})	Expansion coefficient β (M^{-1})
H_2O	1.00	—	18.015	—
H_2O_2	1.45	1.43×10^{-9}	34.015	0.01056
PNPP	1.65	0.209×10^{-9}	371.14	0.1462
PNP	1.27	0.92×10^{-9}	139.11	0.02957
NaH_2PO_4	2.04	0.88×10^{-9}	119.98	0.07092
$(NH_2)_2CO$	1.32	1.38×10^{-9}	60.06	0.01456
$(NH_4)HCO_3$	1.59	1.48×10^{-9}	79.05	0.02933

Table 2 Parameters characterizing the enzymes[48,49]

Enzyme	k_e (s^{-1})	K_M (M)
Acid phosphatase (AP)	26	0.00125
Catalase (CAT)	2.1×10^5	0.093
Urease (UR)	23 000	0.0013

initial concentration of chemicals, or increasing the height of the chamber.

Chemically controlled shape-morphing of an elastic sheet

The simplest chemically active element considered here is a square sheet that is uniformly coated with the enzyme catalase on both the top and bottom surfaces (Fig. 1a). The sheet is 2.25 mm × 2.25 mm in size and the thickness of the sheet is 0.26 mm (see Methods). The initially flat sheet is immersed in an aqueous solution and placed parallel to the bottom wall at a height of $1.2r_0$ above this wall. When hydrogen peroxide (H_2O_2) is uniformly distributed in the chamber, the catalase coating decomposes this reactant into the lighter products, water (H_2O) and oxygen (O_2),

$$H_2O_2 \xrightarrow{\text{Catalase}} H_2O + \frac{1}{2}O_2 \quad (8)$$

Since the solutal expansion coefficient for oxygen is approximately an order of magnitude smaller[36] than that for hydrogen peroxide, we neglect the contribution from the oxygen concentration to the density variation in the solution. Moreover, the reactions rates in this study are sufficiently low that the formation of oxygen bubbles can be ignored.[42] As the products of the reaction are less dense than H_2O_2, solutal buoyancy drives the product-rich fluid to rise upward and generate an inward flow that is directed toward the center of the sheet along the bottom of the chamber. Fig. 1b shows a schematic of the flow lines within a vertical plane passing through the center of the chamber. A similar cross-section in the orthogonal vertical plane also exhibits an inward flow profile so that initially there is a global flow pattern that is symmetric about the center of the chamber. Notably, small changes in the chemical concentration within the microchamber are sufficient to drive fluid flows responsible for the shape changes in the elastic sheet.[34,43]

The fluid flow generated by the enzymatic reaction drives the deformation of the 2D layer into a 3D structure. Since the sheet is uniformly coated with catalyst and characterized by specific values of the bending and stretching moduli, the flow-generated deformation of this 2D sheet yields one particular final 3D form. The 3D form, however, can be tailored by altering the bending modulus, κ_b and stretching modulus, κ_s of the sheet. Fig. 1c and d display the shape-morphing of the sheet into the respective envelope-like, and dome-like structures that are realized for two different values of κ_b (see Movie S1, ESI†).

As indicated by the calculated velocity profiles (marked by black arrows in Fig. 1c and d), the chemically generated inward flows drag the edges (Fig. 1c) or center (Fig. 1d) of the elastic sheet upward. The shape of the elastic sheet is determined by the competition between the elastic forces and the fluid drag. Notably, the edges of the sheet have fewer bounding neighbors than the center of the domain and hence are relatively more flexible than the central region. Thus, for low values of the bending modulus, the edges are sufficiently compliant that the fluid stream moving along the bottom wall and towards the center can drive these edges to fold over into the envelope-like state (Fig. 1c). The bending modulus for this state is $\kappa_b = 0.40$ pN mm^2. For higher bending modulus ($\kappa_b = 0.49$ pN mm^2), the elastic forces are sufficiently high that the sheet can only be deformed by the convergence of all the flow streams at the center of the domain and thus, just the middle of the sheet is distorted by the merging inward flow, which yields the dome-like shape in Fig. 1d. The sheet configurations remain stable for a few hours until the reactant concentration is sufficiently low that the generated convective flow cannot support this shape. After the reagent is depleted, the fluid flow stops and the sheet unfolds and resumes its initial flat configuration.

These different 3D structures can be characterized by the Gaussian and mean curvatures. With two principle curvatures of κ_1 and κ_2 of a surface patch, the Gaussian curvature (K) and mean curvature (H_C) are defined as $K = \kappa_1\kappa_2$ and $H_C = (\kappa_1 + \kappa_2)/2$, respectively. The mean and Gaussian curvatures at each node of the elastic sheet are computed using a model of discretized surfaces[44] (see ESI†). The distributions of Gaussian curvature evaluated at the nodes of the sheet are shown in Fig. 1e and f for the different configurations. The self-folded state has four-fold symmetry in the distributions of Gaussian curvature, while the dome-like state is easily distinguished by the well-defined positive Gaussian curvature at the center of the sheet. Additionally, these different shape morphing structures can be characterized by the distribution of the bending and elastic energy of the sheet (see Fig. S6 and S7, ESI†).

Designing multiple shape transformations with different chemical stimuli

In the above examples, the formation of different 3D shapes was achieved by changing the elastic moduli of the material. Such changes cannot be accomplished ''on the fly'', but rather require alterations to the thickness or constituent materials of the sheet. To overcome this limitation, we develop design rules for creating multiple 3D shape-morphing structures from the same elastic sheet. In particular, the fluid is spatially and temporally ''patterned'' to display non-uniform flows, which permit local and controllable deformations of the sheet. As illustrated by the examples below, the spatio-temporal

patterning of the fluid can be achieved by coating different regions of the sheets and the chamber walls with distinct enzymes and introducing the appropriate chemical stimuli (reactant) that enables specified regions of the chamber to be activated.

Dome-like, bowl-like, and roll-shaped structures

To demonstrate proof-of-principle of these design rules, we consider a square elastic sheet coated with catalase (CAT) and acid phosphatase (AP) in a fluid-filled chamber where two of the side walls are coated with urease (UR) (Fig. 2a). The inner region of the sheet (marked in green) is coated with the catalase and the outer region (marked with red) is coated with the AP. The two side walls marked in yellow are covered with (UR) and the sheet is initially placed at the bottom of this chamber. To create one of the possible shapes, H_2O_2 is introduced into the aqueous solution. Due to the specificity of the catalysts, only the catalase-coated region of the sheet is activated, leading to the decomposition of H_2O_2 into the lighter products (eqn (8)) and the resultant inward flows (indicated by black arrows in Fig. 2b). Hence, the upward movement of the light products above the catalase-coated region of the sheet and the flow along the surface towards the catalase lift the central portion upward, away from the bottom wall. This upward motion morphs the elastic sheet into a dome-like structure (Fig. 2b and Movie S2, ESI†).

The AP-coated outer region of the sheet (marked by red) can be selectively activated by introducing *p*-nitrophenylphosphate hexahydrate (PNPP) into the solution. The enzyme acid phosphatase decomposes PNPN into *p*-nitrophenol (PNP) and monosodium phosphate (NaH_2PO_4),

$$\mathrm{PNPP} \xrightarrow{\text{acid phosphatase}} \mathrm{PNP} + \mathrm{NaH_2PO_4} \qquad (9)$$

The products of this reaction are lighter than the PNPP reactant. In the absence of H_2O_2, the catalase-coated region of the sheet remains chemically inactive. Hence, when PNPP is added to the solution, it is solely the catalytic reaction at the outer region that drives the product rich fluid to move upward and generates inward convective fluid flow at the edges of the sheet. This upwards fluid flow drags these edges away from the bottom, while the chemically inactive central region remains close to the wall. Consequently, the upward movement of the edges gives rise to a bowl-like shape (Fig. 2c and Movie S2, ESI†).

The activation of the catalyst on the coated side walls provides another means of patterning the flow field and thereby morphing the same sheet into yet another 3D structure (Fig. 2d). When urea ($(NH_2)_2CO$) is added to the chamber, the enzyme urease on the side walls (marked by UR) decomposes urea into ammonium bicarbonate (NH_4^+ and HCO_3^- ions),

$$(\mathrm{NH_2})_2\mathrm{CO} \xrightarrow{\text{urease}} \mathrm{NH_4^+} + \mathrm{HCO_3^-} \qquad (10)$$

In this case, the products are denser than the reactant and the motion of the product-rich stream leads to outward flow, moving away from the side walls along the bottom surface. This flow is marked by the black arrows on the non-coated side wall in Fig. 2d. This conversion of reactant to product and resultant flow pattern remains localized near the coated walls

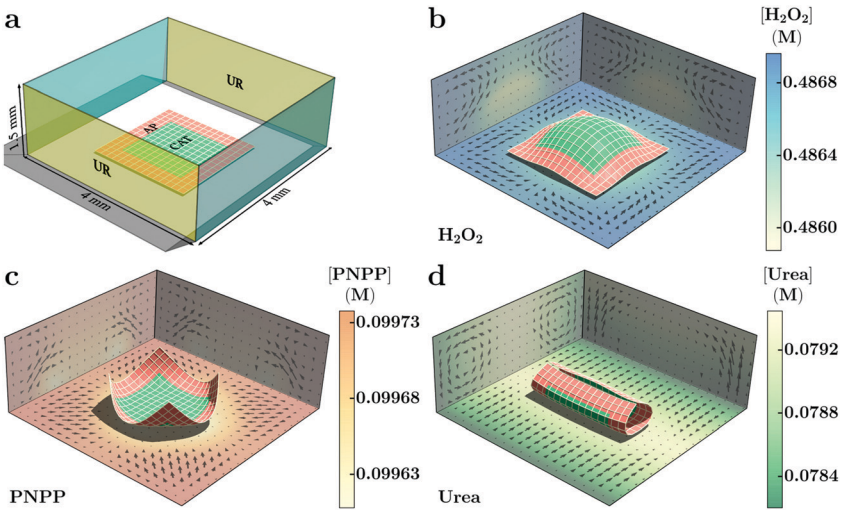

Fig. 2 Multiple shape changes from one sheet in response to different chemical stimuli. (a) Schematic view of a fluid chamber containing a catalase-coated (green region) and acid phosphatase-coated (red) elastic sheet. Two side walls of the fluid chamber are coated with urease (yellow). (b) When the fluid chamber is filled with an aqueous solution of H_2O_2, the reaction on the sheet's surface drives upward fluid flow, which deforms the sheet into the dome-like shape. (c) In the presence of an aqueous solution of PNPP, the upward fluid flow due to the catalytic reaction at the AP-coated region (marked by red) transforms the elastic sheet into a 3D bowl-like structure. (d) With the introduction of an aqueous solution of urea, the two urease-coated side walls (marked by UR in panel (a)) produce a denser product, ammonium bicarbonate. The product rich denser fluid flows downwards close to the side walls and the fluid rises upward away from these side walls. These non-uniform fluid flows morph the sheet into the rolled-shaped structure (see Movie S2, ESI†). The configurations of the elastic sheet in (b–d) are at 390 minutes after the start of the catalytic reaction. The bending and stretching moduli of the sheet are κ_b = 0.22 pN mm^2 and κ_s = 20 pN respectively. Reaction rates are $r^{CAT}_{m,sheet} = 3.6 \times 10^{-6}$ mol m^{-2} s^{-1}, $r^{AP}_{m,sheet} = 4.7 \times 10^{-8}$ mol m^{-2} s^{-1}, and $r^{UR}_{m,sheet} = 1.8 \times 10^{-6}$ mol m^{-2} s^{-1}.

since the enzymatic reaction is confined to this area. This outward flow pushes the two long edges together to yield the roll-shaped structure (Fig. 2d and Movie S2, ESI†).

In the above cases, three distinct shape transformations are achieved from the same chemically-patterned sheet simply by introducing different chemical stimuli. Features of the 3D structures can be tailored by tuning the chemical properties of the sheet. For example, the height of the dome-like state (Fig. 2b) can be controlled by varying the maximal reaction rate of the catalase-catalyzed reaction (Fig. S3, ESI†). In particular, an increase in $r^{\text{enzyme}}_{\text{m,sheet}} = k_e[E]$ generates fluid flows with higher velocities and consequently, greater lift at the center of the sheet (Fig. S3, ESI†). Similarly, the height of the corners of the bowl-like state (Fig. 2c) can be tuned by varying the maximal rate of the AP-catalyzed reaction (Fig. S4, ESI†). The shape of the dome-like or bowl-like state can also be regulated by varying the area and configuration of the catalytic patches.

Wing-like, dome-like, and saddle-shaped structures

Sheets coated with more intricate designs of catalytic patches can yield more complex 3D structures, as demonstrated in Fig. 3a where the elastic sheet is coated with catalase, acid phosphatase, and urease enzymes. Two opposing corners of the sheet are coated with catalase (green patches) and the other two corners are coated with urease (yellow patches). The rest of the surface is coated with acid phosphatase (red patches).

With the addition of H_2O_2 into the chamber, the two catalase-coated corners catalyze the decomposition of H_2O_2 according to the reaction in eqn (8). The other regions of the sheet remain chemically inactive. The resultant inward flow drags the corners upward and gives rise to the wing-like shape in Fig. 3b (Movie S3, ESI†). If only PNPP is added in the chamber, the cross-shaped, AP-coated region becomes activated, while the other portions of the sheet are inactive. The AP-coated regions catalyze the transformation of PNPP to lighter products (*via* the reaction described in eqn (9)). The resultant inward flow is centered at the middle of the sheet (indicated by black arrows in Fig. 3c) and the upward moving stream of fluid transforms the 2D elastic sheet into a dome-like state (Fig. 3c and Movie S3, ESI†).

In the above cases, only one specific enzyme-coated region is chemically activated. To activate all the enzyme-coated regions of the sheet, H_2O_2, PNPP and urea are simultaneously added to the aqueous solution, where the elastically relaxed 2D elastic sheet is placed parallel to the bottom of the chamber (as in Fig. 3a). In the presence of all three reactants, three simultaneous catalytic reactions occur at different patches of the surface of the elastic sheet that transform H_2O_2, PNPP and urea. The decomposition of H_2O_2 into lighter products generates an inward flow at the two opposite CAT-coated corners of the sheet that lifts the two corners upward. At the other corners of the sheet, the decomposition of urea to heavier products generates a downward flow that keeps the two UR-coated corners close to the bottom surface. In addition, the decomposition of PNPP to lighter products creates upward flow at the middle of the sheet that drags the central AP-covered portion of the sheet upward. The combination of these inward and outward flows gives rise to a saddle-shape structure shown in Fig. 3d (see Movie S3, ESI†).

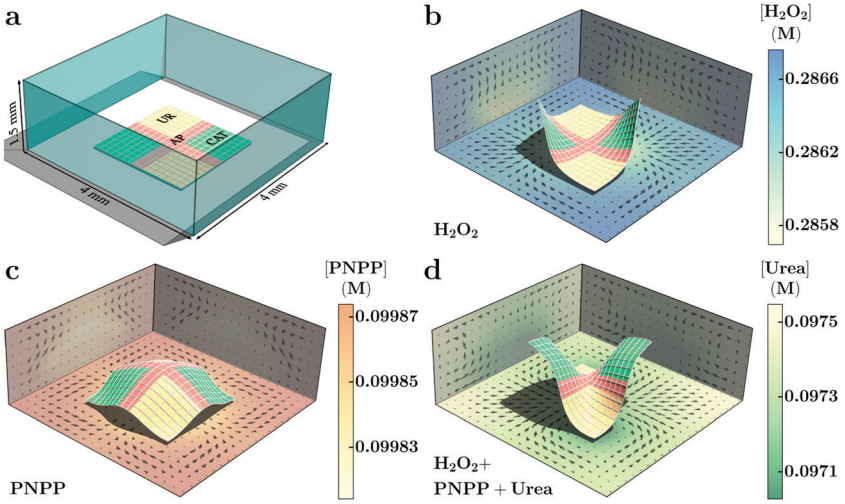

Fig. 3 Designing multiple shape transformations with different chemical stimuli. (a) Schematic view of a fluid chamber containing multiple enzymes coated on an elastic sheet. Two opposite corners are coated with enzymes catalase (green region) and other two corners are coated with urease (yellow region). The rest of the elastic sheet is coated with acid phosphatase (red region). (b) With the introduction of an aqueous solution of H_2O_2, the upward fluid flow at the CAT-coated region drives the sheet into a wing-like shape. (c) In the presence of an aqueous solution of PNPP, the AP-coated region creates upward fluid flow at the center of the sheet that enables the elastic sheet to morph into dome-like structure. (d) With the introduction of an aqueous solution of H_2O_2, PNPP and urea, the combination of the upward fluid flow generated by the catalytic reactions on the catalase-coated and AP-coated regions and downward fluid flow generated by the catalytic reaction on the urease-coated region give rise to this saddle shape structures (see Movie S3, ESI†). The configurations of the elastic sheet in (b)–(d) are respectively at 490, 420 and 236 minutes after the start of the catalytic reaction. The bending and stretching moduli of the sheet are $\kappa_b = 0.22$ pN mm^2 and $\kappa_s = 20$ pN respectively. Reaction rates are $r^{\text{CAT}}_{\text{m,sheet}} = 3.4 \times 10^{-6}$ mol m^{-2} s^{-1}, $r^{\text{AP}}_{\text{m,sheet}} = 5.1 \times 10^{-8}$ mol m^{-2} s^{-1}, and $r^{\text{UR}}_{\text{m,sheet}} = 2.3 \times 10^{-6}$ mol m^{-2} s^{-1}.

Multiple wavy structures

In the third example, we consider a striped, rectangular sheet that can morph into multiple wavy structures in the presence of different chemical stimuli (Fig. 4). The striped, elastic sheet contains catalase-coated (green) and acid-phosphatase coated (red) stripes. The two side walls (marked with UR) are coated with urease. With the introduction of H_2O_2, inward fluid flow is generated at the catalase-coated region (indicated by black arrows in Fig. 4b). This movement of the lighter products drags the catalase-coated regions upward and transforms the flat sheet into a wavy structure (Fig. 4b, Movie S4, ESI†). Initially, the number of peaks in the wavy structure is equal to the number of catalase-coated patches. As the reaction reaches completion, the sheet forms only one central peak due to convective flow about the center of the sheet (see black arrows). By reducing the number of peaks in the sheet and concomitantly increasing the size of the convective vortexes, the system reduces the elastic energy stored in the sheet and the energy dissipated within the fluid. In this wavy structure, the AP-coated edges remain close to the bottom surface of the chamber as the AP-coated region is chemically inactive in the absence of PNPP.

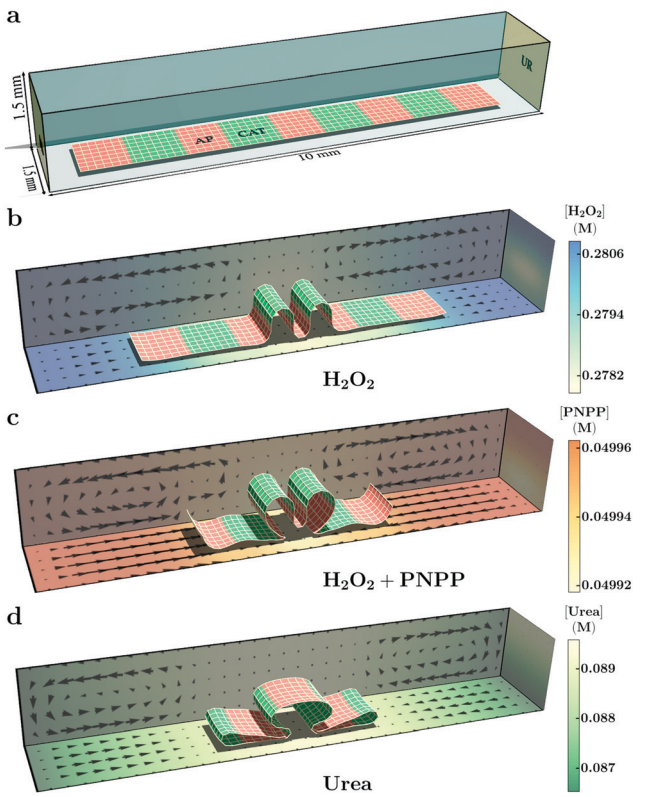

Fig. 4 Designing multiple shape transformations with different chemical stimuli. (a) Schematic view of a fluid chamber containing a rectangular elastic sheet that is coated with catalase (green patches) and acid phosphatase (red patches) to form stripe patterns. Two side walls are coated with urease (yellow region). (b) With the introduction of an aqueous solution of H_2O_2, the upward fluid flow at the catalase-coated region (due to the decomposition of H_2O_2 to lighter products) drives the sheet into a wavy structure with two peaks. (c) In the presence of aqueous solution of PNPP, the AP-coated regions decompose reactant PNPP into lighter products thereby creating an upward fluid flow that morphs the elastic sheet to into a complex wavy-structure. (d) With the introduction of an aqueous solution of urea, the urease-coated two side walls decompose urea to heavier products, which generates downward fluid flow close to the two side walls and upward fluid flow at the middle of the chamber (due to continuity of the flow). This non-uniform convective fluid flow transforms the elastic sheet into a dome-like shape at the middle and roll-shaped structures at the two side ends of the sheet (see Movie S4, ESI†). The configurations of the elastic sheet in (b–d) are at 530 minutes after the start of the catalytic reaction. The bending and stretching moduli of the sheet are $\kappa_b = 0.25$ pN mm^2 and $\kappa_s = 20$ pN respectively. Reaction rates are $r^{CAT}_{m,sheet} = 3.7 \times 10^{-6}$ mol m^{-2} s^{-1}, $r^{AP}_{m,sheet} = 2.1 \times 10^{-8}$ mol m^{-2} s^{-1} and $r^{UR}_{m,sheet} = 1.8 \times 10^{-6}$ mol m^{-2} s^{-1}.

In the presence of both H_2O_2 and PNPP, both the CAT- and AP-coated regions become chemically active and decompose H_2O_2 and PNPP, respectively, to lighter products. The product-rich lighter fluid rises upward above both the CAT and AP patches and the sheet forms the complex wavy structure in Fig. 4c (taken at $t = 530$ min), with the outer AP-coated edges in the upward configuration (Movie S4, ESI†). As in a previous example, we harness the catalytic reaction on the two UR-coated walls by introducing urea into the chamber. In the absence of H_2O_2 and PNPP, the catalase and AP-coated segments are chemically inactive. The short coated walls (Fig. 4a) decompose urea into heavier products, which generate an outward flow. The product-rich outward flow extends along the bottom surface and produces streams (one from each side) that move towards the center of this wall (indicated by black arrows on the bottom wall in Fig. 4d). These streams push the elastic sheet towards this central region and drive the edges of the sheet to fold over on themselves (Movie S4, ESI†).

Lubrication approximation for the initial dynamics of an elastic sheet

To gain additional insight into the early time behavior of the sheet and fluid flow near the sheet, we utilize lubrication theory[45–47] and formulate a 2D description of a thin elastic sheet in a fluid-filled chamber of height H and length L (Fig. 5). Here, the system is described by eqn (23) and (24), presented in the Methods, that govern the dynamics of the sheet, the shape function $h(x,t)$, and reactant concentration, $c(x,t)$. The velocities $\mathbf{u}(x,z,t)$ of the generated convective flows are determined through the functions $h(x,t)$ and $c(x,t)$. The parameters used in the lubrication model are obtained by averaging data from the corresponding simulations (Fig. 2b and 4b) and are summarized in the Methods. In the ensuing figures, the fluid flows are plotted in the spatial units of the layer thickness, H, and lateral domain size, L, but shapes of the sheet $\tilde{h}(\tilde{x},\tilde{t})$ are scaled by the initial sheet position h_0.

We first consider the behavior of the elastic sheet where the central portion is coated with catalase (Fig. 2a). Fig. 6a shows a comparison between the concentration profiles for hydrogen peroxide, $\tilde{c}(\tilde{x},\tilde{t})$, obtained with the lubrication theory (left panels) and the simulations (right panels). The distribution of reactant (Fig. 6a) above the sheet generates an inward flow (Fig. 6c), which deforms the sheet into a dome-like structure (Fig. 6b). The shapes of the profiles $\tilde{h}(\tilde{x},\tilde{t})$ obtained with the

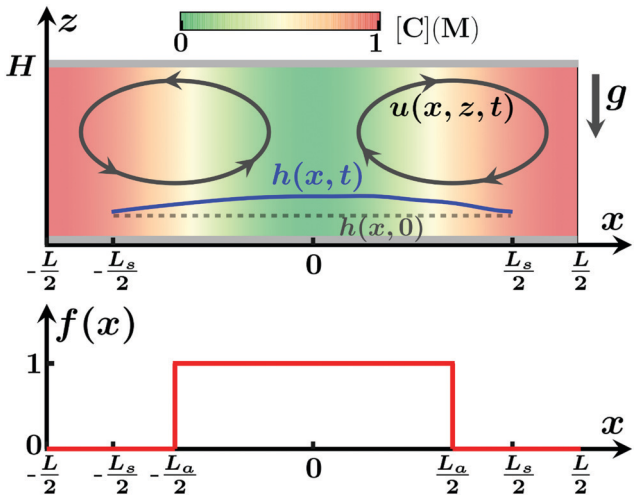

Fig. 5 Schematic of the system analyzed within the lubrication approximation ($L \gg H$). During a chemical reaction promoted by an enzyme localized on the surface of a flexible sheet $h(x,t)$ (blue line), the reactant with concentration $C(x,t)$ is decomposed into lighter products (green). The buoyancy-driven flow, with velocity $\mathbf{u}(x,z,t)$, deforms the sheet $h(x,t)$. The background color illustrates the concentration of the chemical in the chamber. The function $f(x)$ on the bottom panel defines the active portion of the sheet where $f(x) = 1$. Here, L_a is the length of the active region of the sheet.

lubrication model (left) and the simulations (right) show qualitative agreement, with both approaches capturing the upward distension due to the inward flow (Fig. 6c).

Fig. 7a–e show the flow predicted from the lubrication model for time $\tilde{t} = 0.012$ (for the same parameters as in Fig. 6). The distribution of reactant (Fig. 7a) generates two convective vortexes above the sheet (Fig. 7c) that drag the sheet's central region upward. Due to the fluid continuity, the rate of the sheet's upward motion is controlled by the amount of fluid that flows under the sheet from the left and right sides of the domain (Fig. 7e). In response to this influx and flow profile below the sheet, the sheet's edges and central region move downward (Fig. 7b) while the regions around $x/L \approx 0.3$ and $x/L \approx 0.7$ move upward. The profiles of the horizontal $\tilde{u}^-(\tilde{x},0.5\tilde{h},\tilde{t})$ (red) and vertical $\tilde{w}^-(\tilde{x},\tilde{h},\tilde{t})$ (black) components of the fluid velocity below the sheet (Fig. 7d) emphasize that the spatial variations in the fluid correlate with local displacements and deformations of the sheet. Namely, the horizontal component, $\tilde{u}^-$, of the fluid velocity goes through zero and changes sign while the vertical component, $\tilde{w}^-$, attains negative values at the central region (Fig. 7d and f).

The lubrication model reveals that the early dynamic behavior of the sheet is controlled by the sheet's initial distance from the bottom wall, h_0. Specifically, Fig. S5 (ESI†) reveals that for the same dimensionless time $\tilde{t}$, sheets closer to the bottom wall are more slowly deformed by the imposed fluid drag. Fluid fluxes from the two side walls (and flowing beneath the sheet) are smaller for sheets closer to the bottom wall, accounting for the smaller deformations of the latter samples. Additionally, the smaller gap between the moving sheet and the bottom wall introduces larger fluid shear stresses that act to slow down the structural evolution of the sheet.

We extend our theoretical model to examine sheets that are not uniformly coated with catalyst, but encompass multiple, finite-sized catalytic patches. We consider a rectangular elastic sheet with a pattern similar to that shown in Fig. 4a, however, the space previously occupied by AP is now left uncoated.

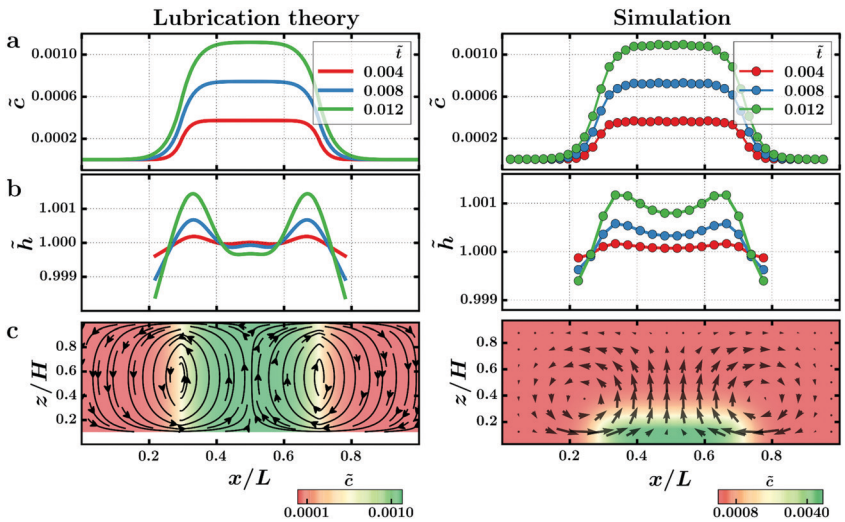

Fig. 6 Comparison of the initial dynamics of the sheet obtained with the lubrication approximation (left panels) and simulations (right panels) for initial sheet locations $h_0 = 0.15$ mm. (a) Top panels show the concentration variations along the chamber for three different instances of time. The concentration profile for the simulation is calculated as the average concentration of H_2O_2 over the depth of the chamber, $\int_0^1 \tilde{c}(\tilde{x},\tilde{y}=0.5,\tilde{z},\tilde{t})\mathrm{d}\tilde{z}$. The two profiles show quantitative agreement for all three times. (b) Profiles of the sheet obtained with the lubrication model (left panels) and simulations (right panels). (c) Fluid flow above the sheet ($y/L = 0.5$ in the simulations). In both the cases, the chemically active middle region spans 75% of the total area of the sheet. The dimensionless numbers, defined in the Methods, are Ra = 1.0, $B = 2.1 \times 10^{-7}$, $\tilde{D} = 0.19$, and $Q = 0.19$. Results for three different dimensionless times are shown in red, blue, and green and correspond to physical times $t = 8$, 17, and 25 s.

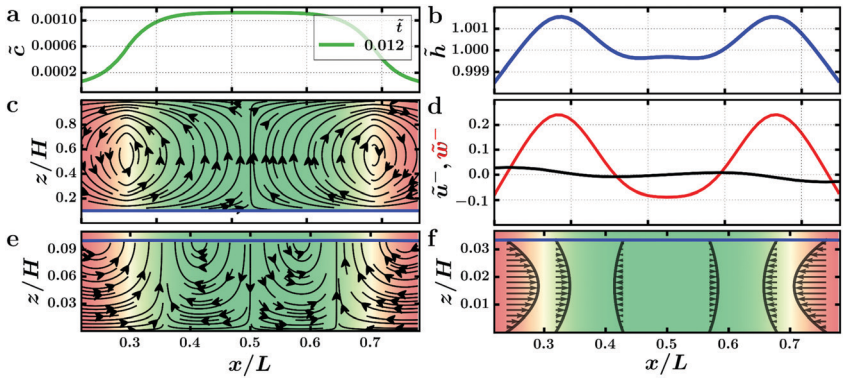

Fig. 7 Initial dynamics of the elastic sheet and fluid flow obtained from the lubrication approximation for initial sheet position h_0 = 0.15 mm at time, $\tilde{t}$ = 0.012. The sheet's chemically active middle portion is located in the interval $0.3 \leq x/L \leq 0.7$. (a) Profile of the reactant concentration $\tilde{c}(\tilde{x},\tilde{t})$. (b) Shape of the sheet $\tilde{h}(\tilde{x},\tilde{t})$. (c and e) Fluid flows above (c) and below (e) the sheet are shown with the streamlines and black arrows. Blue line shows the location of the sheet $\tilde{h}(\tilde{x},\tilde{t})$. (d) Horizontal $\tilde{u}^-(\tilde{x},\tilde{z} = 0.5\tilde{h},\tilde{t})$ (black line) and vertical $\tilde{w}^-(\tilde{x},\tilde{z} = \tilde{h},\tilde{t})$ (red line) components of the fluid velocity below the sheet. (f) Horizontal fluid flow profile $\tilde{u}^-(\tilde{x},\tilde{z},\tilde{t})$ below the sheet reveals the inward fluid flow towards the center.

We use the same parameters for the catalytic reactions and sizes of the catalyst-coated regions in the lubrication theory and simulations. Fig. 8 shows the concentration profiles $\tilde{c}(\tilde{x},\tilde{t})$ (Fig. 8a), the shape of the sheets (Fig. 8b), and the structures of the flow (Fig. 8c) for this multi-patched catalase-coated sheet obtained with both approaches. The periodic arrangement of the catalase-coated regions produces a periodic distribution of the concentration of H_2O_2 (Fig. 8a), as well as a four-peak structure of the sheet profile (Fig. 8b). The flow pattern exhibits two vortices of inward flow that are centered above each catalase-coated patch, as is apparent in both panels of Fig. 8c. The component of this inward flow that moves along the sheet's surface and toward each side of a patch (see Fig. 8c) drags the sides of each patch inward and the upward flow above the center of a patch pulls this region upward. The combined drag imposed by these flows on the sheet produces the buckled pattern seen in both panels of Fig. 8b, which shows quantitative agreement between the lubrication theory and simulation.

Discussion

We demonstrated the controllable shape transformations of chemically active, two-dimensional sheets into well-defined three-dimensional structures in response to the appropriate chemical stimulus. A unique feature of these shape transformations is that they are driven by inherent phenomena that happen spontaneously when catalytic reactions occur in confined fluids. Namely, catalytic reactions at surfaces generate density gradients and thereby produce intrinsic solutal buoyancy forces

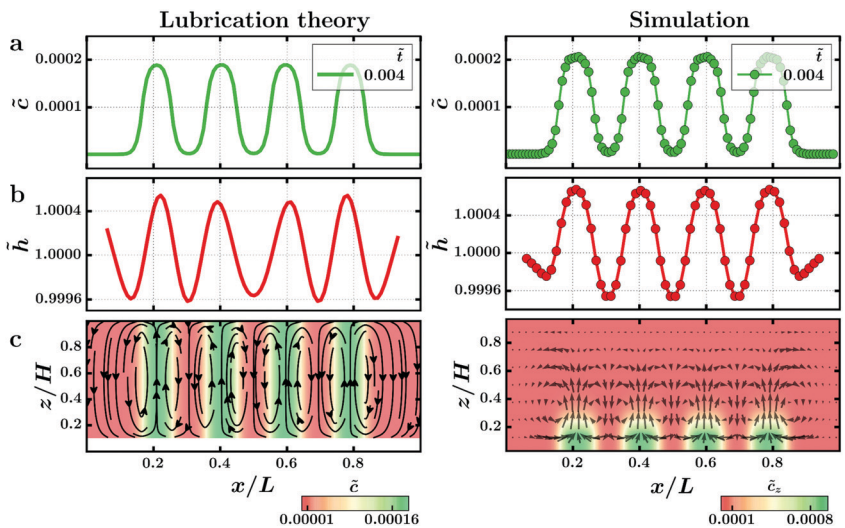

Fig. 8 Initial dynamics of the elastic sheet with multi-patches active patches obtained within lubrication approximation (left panels) and simulations (right panels) h_0 = 0.15 mm. The geometry and locations of four catalase-coated patches are the same as in the case in Fig. 4(a). (a) Top panels show variations of the concentration $\tilde{c}(\tilde{x},\tilde{t})$ along the chamber at the time $\tilde{t}$ = 0.004. (b) The sheet profiles with four peaks obtained in the lubrication model (left panel) and simulations (right panel). (c) Bottom panels show the fluid vortices above the sheet. Dimensionless parameters for the lubrication model are taken Ra = 1.0, $B = 6 \times 10^{-8}$, $\tilde{D}$ = 0.06, and Q = 0.06.

(for the cases considered here). The latter forces act on the surrounding solution to propel the flow of the confined fluids. The fluids in turn exert forces on thin, compliant layers immersed in the solution. Hence, with the addition of the reactant that initiates the catalytic reaction, the system itself generates the chain of interconnected, dynamic events that lead to the desired shape transformations of immersed, flexible sheets. In this sense, the shape transformations occur through a distinctive self-contained process.

Another distinctive feature of this system is that the spatio-temporal features of the fluid flow can be patterned through the choice and placement of the catalyst in a microchamber. Thus the forces acting on the immersed sheet can be tuned to yield the specific 3D morphology needed for a particular application. Here, the catalysts are localized on the surface of the sheets so that sheets themselves generate the necessary forces for their transformation.

The desired 3D forms can be achieved by patterning the arrangement of the catalytic domains on the sheet and introducing the appropriate reactant to initiate one or more of the specific catalytic reactions. As proof of principle, we showed how a single sheet that encompasses multiple catalytic domains can be transformed into a variety of 3D shapes through the addition of a particular reactant or the simultaneous addition of all the reactants.

Notably, the 3D shapes can be tailored by altering the flexibility and shapes of the elastic sheets, as well as the geometry of the fluid-filled container. Here, we showed that sheets differing solely in their elastic properties morphed into distinct geometries, depending on the stretching and bending moduli of the layer. For a sheet with a given coating, shape and flexibility, different shape-changes could be induced by placing the sheet into containers with different geometries since the walls of the chamber strongly influence the velocities of the generated convective flows. Additional structural transformations could be induced through the use of cascade reactions, where the product of one reaction is the reactant for the next. Cascade reactions provide an effective means of controlling the spatio-temporal patterns in the fluid flows[34] and hence can lead to yet different forms of shape-changing. These design rules can guide the creation of adaptive, soft robots and chemical sensors operating in a self-sustained manner and thus facilitate the development of portable, multifunctional of fluidic devices.

Methods

Numerical simulations

A lattice Boltzmann method (LBM) with a single relaxation-time D3Q19 scheme is used to solve the continuity and Navier–Stokes equations (eqn (2) and (3)) at each time step of the simulation. The reaction-diffusion equation (eqn (4)) is solved using a finite difference approach with a forward-time central-space (FTCS) scheme. The immersed boundary (IB) approach is used to capture the fluid–structure interactions between elastic sheet and fluid. In the IB model, each node of the elastic sheet is represented by a sphere with effective hydrodynamics radius a that experiences fluid drag, characterized by the mobility $\mu = (6\pi\eta a)^{-1}$. Thus, the effective thickness of the elastic sheet is equal to the diameter $2a$ of a single node. We keep the thickness of the sheet constant and vary the elastic modulus to alter the mechanical properties of the sheet. The forces $\mathbf{F}_{el}$ exerted by the nodes of the elastic sheet on the fluid, calculated using the IB method, provide zero fluid velocities at the discretized nodes of the elastic sheet. Therefore, the IB approach approximates no-slip conditions for the fluid velocities at the nodes' boundaries, as well as no fluid permeation through the nodes of the sheet. Moreover, all these nodes are assumed to have the same chemical activity, which is proportional to SK_d (see eqn (4)).

The velocity field $\mathbf{u}(u_x,u_y,u_z)$ computed using the LBM method is used to advect the chemical concentration (eqn (4)) and to update the position of nodes of the elastic sheet (eqn (5)). The updated concentration field is then used to determine the buoyancy forces in eqn (3). To simulate the shape morphing of the sheet, this procedure is repeated for 2×10^7 steps, which correspond to approximately 9 hours. The time step size, Δt, in the simulation is 1.67×10^{-3} s.

The size of the computational domain for Fig. 1–3 and Fig. 4 are $42\Delta x \times 42\Delta x \times 17\Delta x$ and $102\Delta x \times 17\Delta x \times 17\Delta x$, respectively, where the lattice Boltzmann unit Δx is 100 μm. Thus, the physical dimensions of these two simulation boxes are 4 mm × 4 mm × 1.5 mm and 10 mm × 1.5 mm × 1.5 mm, respectively. In the discretization of the elastic sheet, the distance between two nearest neighboring nodes is set to $1.5\Delta x$. The lateral dimensions of the elastic sheet in Fig. 1–3 and Fig. 4 are 2.25 mm × 2.25 mm and 8.85 mm × 1.05 mm, respectively, and 0.26 mm in thickness. The equilibrium distance characterizing the Morse potential (eqn (1)), r_0 is taken as $1.3\Delta x$.

Lubrication approximation

In the lubrication approximation,[45–47] we use a shape function $h(x,t)$ to characterize the dynamics of the neutrally buoyant sheet, which initially is suspended at the distance $h(x,0) = h_0$ from the bottom wall. The geometry of the system under consideration is shown in Fig. 5. We assume that $H \gg h(x,t)$, which implies that sheet lies near the bottom wall, and $\left|\frac{\partial h(x,t)}{\partial x}\right| \sim \frac{h}{L} \ll 1$, which specifies that the slopes characterizing variations in shape are small. The latter assumption is applied during the entire structural evolution. The sheet's shape is determined by a balance between the elastic forces and pressure above ($p+$) and below ($p-$) the sheet. Consequently, the quasi-steady shape (neglecting the inertia of the sheet) can be calculated from the beam equation:[50]

$$F\frac{\partial^4 h}{\partial x^4} = -p^+ + p^-. \quad (11)$$

Note that values of F are related to the bending modulus κ_b used in the simulations through the expression $F = \kappa_b/b_0$, where b_0 is the distance between two nearest neighbor nodes of

the sheet. We assume that the solutal buoyancy-driven fluid flow is sufficiently slow and the corresponding Reynolds number is sufficiently small that the fluid velocity $\mathbf{u} = (u(x,z,t),w(x,z,t))$ above the sheet ($z > h(x,t)$) can be described by the continuity and Stokes equations. In the lubrication approximation, these equations become:

$$\frac{\partial u^+}{\partial x} + \frac{\partial w^+}{\partial z} = 0. \tag{12a}$$

$$\frac{\partial p^+}{\partial z} = -g\rho_0\beta C(x,t). \tag{12b}$$

$$\frac{\partial p^+}{\partial x} = \mu\frac{\partial^2 u^+}{\partial z^2}, \quad h \le z \le H. \tag{12c}$$

Analogously, in the region below the sheet ($0 < z < h(x,t)$), the fluid velocity satisfies:

$$\frac{\partial u^-}{\partial x} + \frac{\partial w^-}{\partial z} = 0, \tag{13a}$$

$$\frac{\partial p^-}{\partial z} = 0, \tag{13b}$$

$$\frac{\partial p^-}{\partial x} = \mu\frac{\partial^2 u^-}{\partial z^2}, \quad 0 \le z \le h. \tag{13c}$$

The dynamics of the sheet is controlled by the fluid drag imposed on the sheet by the fluid flows and the velocities of the buoyancy-generated convection are known to strongly depend on the thickness of the liquid layer. Therefore, in the limit $h(x,t) \ll H$, we neglect the buoyancy effects below the elastic sheet, which is assumed to be impermeable to the fluid.

We assume that the sheet is coated with an enzyme that decomposes a reactant into less dense products. For simplicity, we consider the decomposition of one chemical reactant of concentration c. In the limit of small Peclet numbers $\left(\frac{Lu}{D}\right)$ and in a domain where the horizontal length-scale is much larger than the vertical one, the evolution of the reactant $c(t,x)$ can be described by the equation

$$\frac{\partial c}{\partial t} = D\frac{\partial^2 c}{\partial x^2} - r\frac{c}{K_M + c}f(x), \tag{14}$$

where D is the diffusivity. The reaction rate $r = [E]k$ (mol m^{-3} s^{-1}) involves the reaction rate of a single enzyme molecule k (s^{-1}) and the concentration of the enzyme [E] (mol m^{-3}). K_M is the Michaelis constant of the corresponding enzymatic reaction. The function $f(x)$ describes the shape of the catalytic area on the sheet (see Fig. 5),

$$f(x) = \begin{cases} 1 & -L_a/2 \le x \le L_a/2 \\ 0 & \text{otherwise} \end{cases}.$$

At the solid walls that bound the domain, we impose no-slip boundary conditions ($\mathbf{u} = 0$) and zero flux for the chemical concentrations $\left(\frac{\partial c}{\partial \mathbf{n}} = 0\right)$, where $\mathbf{n}$ is the normal vector to the wall.

Integrating eqn (12b) and (13b), and using the relationship between p^+ and p^- (eqn (11)), the pressure above and below the sheet can be presented as

$$\begin{aligned} p^+(x,z,t) &= p^0(x,t) + g\rho_0\beta c(x,t)(H-z), \\ p^-(x,t) &= p^0(x,t) + g\rho_0\beta c(x,t)(H-h) + F\partial^4 h/\partial x^4, \end{aligned} \tag{15}$$

where the function $p^0(x,t)$ is determined from the requirement of a zero fluid flux across the vertical section of the chamber (see further below). Integrating eqn (12c) and (13c) for velocities and using the no-slip boundary conditions ($u = 0$ and $w = 0$) on the walls, the horizontal velocities are given as

$$u^+(x,z,t) = \frac{(h-z)(z-H)}{6\mu}\left(g\rho_0\beta c_x(h-2H+z) - 3p_x^0\right), \tag{16a}$$

$$u^-(x,z,t) = -\frac{(h-z)z}{2\mu}\left(F\frac{\partial^5 h}{\partial x^5} + p_x^0 + g\rho_0\beta(c_x(H-h) - ch_x)\right). \tag{16b}$$

Integrating the continuity equations above and below the sheet (eqn (12a) and (13a)), expressions for the vertical fluid velocities can be derived through the horizontal components $u^+(x,z,t)$ and $u^-(x,z,t)$ as

$$w^+(x,z,t) = \int_z^H \frac{\partial u^+(x,z',t)}{\partial x}\mathrm{d}z' \text{ and } w^-(x,z,t) = -\int_0^z \frac{\partial u^-(x,z',t)}{\partial x}\mathrm{d}z'. \tag{17}$$

From the equality of the two vertical velocities $w^+(x,z,t) = w^-(x,z,t)$ at the location of the sheet, $z = h(x,t)$, the function p_x^0 is obtained as:

$$p_x^0 = \frac{1}{(h-H)^3 - h^3} \times \left\{h^3 F\frac{\partial^5 h}{\partial x^5} + \frac{g\rho_0\beta}{2}\left[-2ch^3h_x + c_x(h-H)\left(-2h^3 + (h-H)^3\right)\right]\right\}. \tag{18}$$

The kinematic condition $\partial h(x,t)/\partial t = w^-(x,h(x,t),t)$ provides the equation governing the dynamics of the flexible sheet

$$\frac{\partial h}{\partial t} = \frac{1}{12\mu}\frac{\partial}{\partial x}\left[\frac{h^3(h-H)^3}{(h-H)^3 - h^3}\left(F\partial_x^5 h - \frac{g\rho_0\beta}{2}(2ch_x + c_x(h-H))\right)\right]. \tag{19}$$

This equation is supplemented by the diffusion equation describing the transport of the reactant

$$\frac{\partial c}{\partial t} = D\frac{\partial^2 c}{\partial x^2} - r\frac{c}{K_M + c}f(x). \tag{20}$$

The sixth- and second-order partial differential equations, eqn (19) and (20), are supplemented with the appropriate

boundary conditions and initial conditions:

$$x=-L_S/2: h_{xx}=h_{xxx}=h_{xxxx}=0,\ x=L_S/2: h_{xx}=h_{xxx}=h_{xxxx}=0.$$

$$x=-L/2: c_x=0,\ x=L/2: c_x=0.$$

$$h(x,t=0)=h_0,\ c(x,t=0)=c_{ini} \tag{21}$$

Here, L and L_S are the lengths of the chamber and sheet, respectively. We assumed that there is no bending moment (h_{xx} = 0) and shearing force (h_{xxx} = 0) acting at the ends of the sheet. The fourth derivative of height (h_{xxxx} = 0) at the two ends of the sheet models the assumption that the pressures above and below the sheet are equal.

Next, we introduce dimensionless variables marked with tildes

$$h=\tilde{h}h_0,\ t=\tilde{t}\tau,\ x=\tilde{x}L,\ c=c_{ini}-\tilde{c}C_0 \tag{22}$$

and rewrite eqn (19) and (20) in the form

$$\frac{\partial\tilde{h}}{\partial\tilde{t}}=\frac{\partial}{\partial\tilde{x}}\left[\frac{\tilde{h}^3\left(\tilde{h}-H/h_0\right)^3}{\left(\tilde{h}-H/h_0\right)^3-\tilde{h}^3}\times\left(B\frac{\partial^5\tilde{h}}{\partial\tilde{x}^5}-\mathrm{Ra}\left(2\frac{h_0}{H}\left(\frac{c_{ini}}{C_0}-\tilde{c}\right)\tilde{h}_{\tilde{x}}+\tilde{c}_{\tilde{x}}\left(1-\frac{h_0}{H}\tilde{h}\right)\right)\right)\right], \tag{23}$$

$$\frac{\partial\tilde{c}}{\partial\tilde{t}}=\tilde{D}\frac{\partial^2\tilde{c}}{\partial\tilde{x}^2}-Q\frac{c_{ini}/C_0-\tilde{c}}{(K_M+c_{ini})/C_0-\tilde{c}}f(\tilde{x}), \tag{24}$$

where we introduced the dimensionless ratios

$$B=\frac{\tau h_0^3F}{12\mu L^6},\quad \mathrm{Ra}=\frac{\tau g\rho_0\beta C_0h_0^2H}{24\mu L^2},\quad \tilde{D}=\frac{\tau D}{L^2},\quad Q=\frac{\tau r}{C_0}. \tag{25}$$

The system is characterized by a number of different time scales; these time scales involve elastic $\tau_B=\frac{12\mu L^6}{h_0^3F}$, viscous $\tau_{Ra}=\frac{24\mu L^2}{\rho_0g\beta C_0h_0^3}$, diffusive $\tau_D=\frac{L^2}{D}$, and reactive $\tau_Q=\frac{C_0}{r}$ effects. The dimensionless numbers (top row) can then be expressed in terms of these time scales (left column) as summarized in Table 3.

We choose the following values for parameters representative of the numerical simulations: K_M = 100 mol m^{-3}, h_0 = 0.15 mm, H = 1.5 mm, L = 4 mm, F = 1.5 × 10^{-15} kg m^2 s^{-2}, g = 9.81 m s^{-2} μ = 10^{-3} kg m^{-1} s^{-1}, ρ = 10^3 kg m^{-3}, β = 10^{-5} m^3 mol^{-1}, D = 1.43 × 10^{-9} m^2 s^{-1}, r = 0.005 mol m^{-3} s^{-1} and $C_0=rL^2/D$ = 55.6 mol m^{-3}. These choices lead to the values for the dimensionless numbers listed in Table 4, where different choices of the characteristic time influences the magnitude of the dimensionless ratios.

Even though at all the time scales $B \ll$ Ra, it is important to keep the term proportional to B in the film equation, eqn (23), because without this term (which multiplies the highest derivative term) the profile of the sheet develops unphysical sharp kinks.

We choose the viscous time scale to be $\tau_{Ra}=\frac{24\mu L^2}{\rho_0g\beta C_0h_0^2H}$, which ensures Ra = 1. The time scale τ_{Ra}, together with dimensionless parameters B, $\tilde{D}$, and Q, are functions of the initial distance of the sheet from the bottom wall h_0. We solve the coupled equations eqn (23) and (24) numerically. In these

Table 3 Dimensionless parameters

	$B=\frac{\tau h_0^3F}{12\mu L^6}$	$\mathrm{Ra}=\frac{\tau g\rho_0\beta C_0h_0^2H}{24\mu L^2}$	$\tilde{D}=\frac{\tau D}{L^2}$	$Q=\frac{\tau r}{C_0}$
$\tau_B=\frac{12\mu L^6}{h_0^3F}$	$B=1$	$\mathrm{Ra}=\frac{g\rho_0\beta C_0L^4H}{2Fh_0}$	$\tilde{D}=\frac{12\mu L^4D}{h_0^3F}$	$Q=\frac{12\mu L^6}{h_0^3F}\frac{r}{C_0}$
$\tau_{Ra}=\frac{24\mu L^2}{\rho_0g\beta C_0h_0^2H}$	$B=\frac{2Fh_0}{\rho_0g\beta C_0L^4H}$	Ra = 1	$\tilde{D}=\frac{24\mu D}{\rho_0g\beta C_0h_0^2H}$	$Q=\frac{24\mu L^2r}{\rho_0g\beta C_0^2h_0^2H}$
$\tau_D=\frac{L^2}{D}$	$B=\frac{h_0^3F}{12D\mu L^4}$	$\mathrm{Ra}=\frac{g\rho_0\beta C_0h_0^2H}{24D\mu}$	$\tilde{D}=1$	$Q=\frac{L^2}{D}\frac{r}{C_0}$
$\tau_Q=\frac{C_0}{r}$	$B=\frac{C_0}{r}\frac{h_0^3F}{12\mu L^6}$	$\mathrm{Ra}=\frac{g\rho_0\beta C_0^2h_0^2H}{24r\mu L^2}$	$\tilde{D}=\frac{C_0}{r}\frac{D}{L^2}$	$Q=1$

Table 4 Values of the parameters

	$B=\frac{\tau h_0^3F}{12\mu L^6}$	$\mathrm{Ra}=\frac{\tau g\rho_0\beta C_0h_0^2H}{24\mu L^2}$	$\tilde{D}=\frac{\tau D}{L^2}$	$Q=\frac{\tau r}{C_0}$
τ_B = 9.7 × 10^9 s	B = 1	Ra = 4.7 × 10^6	$\tilde{D}$ = 8.7 × 10^5	$\tilde{D}$ = 8.7 × 10^5
τ_{Ra} = 2.1 × 10^3 s	B = 2.1 × 10^{-7}	Ra = 1	$\tilde{D}$ = 0.19	Q = 0.19
τ_D = 1.1 × 10^4 s	B = 1.1 × 10^{-6}	Ra = 5.4	$\tilde{D}$ = 1	Q = 1
τ_Q = 1.1 × 10^4 s	B = 1.1 × 10^{-6}	Ra = 5.4	$\tilde{D}$ = 1	Q = 1

units, the results for h_0 = 0.15 mm shown in the plots are obtained over the dimensionless time interval $0 \leq \tilde{t} \leq 0.012$.

Author contributions

All authors designed the system described here and determined the studies to be performed. R. K. M. and O. E. S. performed the simulations and numerical calculations. All the authors helped analyze the data and contributed to writing the manuscript.

Conflicts of interest

There are no conflicts to declare.

Acknowledgements

A. C. B. gratefully acknowledges funding from DOE under grant number DE-FG02-90ER45438, which supported the development of the computational work. A. C. B. and H. A. Stone gratefully acknowledge funding from NSF grant 1740630, which supported the development of the analytical theory. We acknowledge the computational facilities at the Center for Research Computing at the University of Pittsburgh. The authors also thank Bhargav Rallabandi for useful discussions of the lubrication theory.

References

1 R. M. Erb, J. S. Sander, R. Grisch and A. R. Studart, Self-Shaping Composites with Programmable Bioinspired Microstructures, *Nat. Commun.*, 2013, **4**, 1–8, DOI: 10.1038/ncomms2666.

2 A. R. Studart, Biologically Inspired Dynamic Material Systems, *Angew. Chem., Int. Ed.*, 2015, **54**(11), 3400–3416, DOI: 10.1002/anie.201410139.

3 T. van Manen, S. Janbaz and A. A. Zadpoor, Programming the Shape-Shifting of Flat Soft Matter, *Mater. Today*, 2018, **21**(2), 144–163, DOI: 10.1016/j.mattod.2017.08.026.

4 J. Dervaux and M. Ben Amar, Morphogenesis of Growing Soft Tissues, *Phys. Rev. Lett.*, 2008, **101**(6), 1–4, DOI: 10.1103/PhysRevLett.101.068101.

5 U. Nath, B. C. W. Crawford, R. Carpenter and E. Coen, Genetic Control of Surface Curvature. [Science. 2003] - PubMed Result, *Science*, 2003, **299**(5611), 1404–1407, DOI: 10.1126/science.1079354.

6 M. Wehner, R. L. Truby, D. J. Fitzgerald, B. Mosadegh, G. M. Whitesides, J. A. Lewis and R. J. Wood, An Integrated Design and Fabrication Strategy for Entirely Soft, Autonomous Robots, *Nature*, 2016, **536**(7617), 451–455, DOI: 10.1038/nature19100.

7 T. Li, G. Li, Y. Liang, T. Cheng, J. Dai, X. Yang, B. Liu, Z. Zeng, Z. Huang and Y. Luo, *et al.*, Fast-Moving Soft Electronic Fish, *Sci. Adv.*, 2017, **3**(4), 1–7, DOI: 10.1126/sciadv.1602045.

8 S. Y. Kim, R. Baines, J. Booth, N. Vasios, K. Bertoldi and R. Kramer-Bottiglio, Reconfigurable Soft Body Trajectories Using Unidirectionally Stretchable Composite Laminae, *Nat. Commun.*, 2019, **10**(1), 1–8, DOI: 10.1038/s41467-019-11294-7.

9 J. C. Breger, C. Yoon, R. Xiao, H. R. Kwag, M. O. Wang, J. P. Fisher, T. D. Nguyen and D. H. Gracias, Self-Folding Thermo-Magnetically Responsive Soft Microgrippers, *ACS Appl. Mater. Interfaces*, 2015, **7**(5), 3398–3405, DOI: 10.1021/am508621s.

10 X. Yang, C. An, S. Liu, T. Cheng, V. Bunpetch, Y. Liu, S. Dong, S. Li, X. Zou and T. Li, *et al.*, Soft Artificial Bladder Detrusor, *Adv. Healthcare Mater.*, 2018, **7**(6), 1–9, DOI: 10.1002/adhm.201701014.

11 B. Gorissen, D. Reynaerts, S. Konishi, K. Yoshida, J. W. Kim and M. De Volder, Elastic Inflatable Actuators for Soft Robotic Applications, *Adv. Mater.*, 2017, **29**(43), 1–14, DOI: 10.1002/adma.201604977.

12 M. Jamal, S. S. Kadam, R. Xiao, F. Jivan, T. M. Onn, R. Fernandes, T. D. Nguyen and D. H. Gracias, Bio-Origami Hydrogel Scaffolds Composed of Photocrosslinked PEG Bilayers, *Adv. Healthcare Mater.*, 2013, **2**(8), 1142–1150, DOI: 10.1002/adhm.201200458.

13 M. Betsch, C. Cristian, Y. Y. Lin, A. Blaeser, J. Schöneberg, M. Vogt, E. M. Buhl, H. Fischer and D. F. Duarte Campos, Incorporating 4D into Bioprinting: Real-Time Magnetically Directed Collagen Fiber Alignment for Generating Complex Multilayered Tissues, *Adv. Healthcare Mater.*, 2018, **7**(21), 1–9, DOI: 10.1002/adhm.201800894.

14 A. Lendlein and R. Langer, Biodegradable, Elastic Shape-Memory Polymers for Potential Biomedical Applications, *Science*, 2002, **296**(5573), 1673–1676, DOI: 10.1126/science.1066102.

15 T. M. Conjugated and R. Langer, Light-Induced Shape-Memory Polymers, *Nature*, 2005, **434**, 695–697, DOI: 10.1038/nature03438.1.

16 Y. Klein, E. Efrati and E. Sharon, Shaping of Elastic Sheets By, *Science*, 2007, **9**, 1116–1120, DOI: 10.1126/science.1137920.

17 J. Kim, J. A. Hanna, M. Byun, C. D. Santangelo and R. C. Hayward, Surfaces by Halftone Gel Lithography, *Science*, 2012, **1201**, 1200–1205, DOI: 10.1126/science.1215309.

18 A. Sydney Gladman, E. A. Matsumoto, R. G. Nuzzo, L. Mahadevan and J. A. Lewis, Biomimetic 4D Printing, *Nat. Mater.*, 2016, **15**(4), 413–418, DOI: 10.1038/nmat4544.

19 O. Erol, A. Pantula, W. Liu and D. H. Gracias, Transformer Hydrogels: A Review, *Adv. Mater. Technol.*, 2019, **4**(4), 1–27, DOI: 10.1002/admt.201900043.

20 T. J. White and D. J. Broer, Programmable and Adaptive Mechanics with Liquid Crystal Polymer Networks and Elastomers, *Nat. Mater.*, 2015, **14**(11), 1087–1098, DOI: 10.1038/nmat4433.

21 Y. Yao, J. T. Waters, A. V. Shneidman, J. Cui, X. Wang, N. K. Mandsberg, S. Li, A. C. Balazs and J. Aizenberg, Multiresponsive Polymeric Microstructures with Encoded Predetermined and Self-Regulated Deformability, *Proc. Natl. Acad. Sci. U. S. A.*, 2018, **115**(51), 12950–12955, DOI: 10.1073/pnas.1811823115.

22 J. H. Na, A. A. Evans, J. Bae, M. C. Chiappelli, C. D. Santangelo, R. J. Lang, T. C. Hull and R. C. Hayward, Programming Reversibly Self-Folding Origami with Micropatterned Photo-Crosslinkable Polymer Trilayers, *Adv. Mater.*, 2015, **27**(1), 79–85, DOI: 10.1002/adma.201403510.

23 H. Zhang, X. Guo, J. Wu, D. Fang and Y. Zhang, Soft Mechanical Metamaterials with Unusual Swelling Behavior and Tunable Stress-Strain Curves, *Sci. Adv.*, 2018, **4**(6), 1–11, DOI: 10.1126/sciadv.aar8535.

24 L. Huang, R. Jiang, J. Wu, J. Song, H. Bai, B. Li, Q. Zhao and T. Xie, Ultrafast Digital Printing toward 4D Shape Changing Materials, *Adv. Mater.*, 2017, **29**(7), 1–6, DOI: 10.1002/adma.201605390.

25 A. Nojoomi, H. Arslan, K. Lee and K. Yum, Bioinspired 3D Structures with Programmable Morphologies and Motions, *Nat. Commun.*, 2018, **9**(1), 1–11, DOI: 10.1038/s41467-018-05569-8.

26 S. J. Jeon, A. W. Hauser and R. C. Hayward, Shape-Morphing Materials from Stimuli-Responsive Hydrogel Hybrids, *Acc. Chem. Res.*, 2017, **50**(2), 161–169, DOI: 10.1021/acs.accounts.6b00570.

27 L. Ionov, 4D Biofabrication: Materials, Methods, and Applications, *Adv. Healthcare Mater.*, 2018, **7**(17), 1–14, DOI: 10.1002/adhm.201800412.

28 M. Ma, L. Guo, D. G. Anderson and R. Langer, By Water Gradients, *Science*, 2013, **339**(6116), 186–189, DOI: 10.1126/science.1230262.Bio-inspired.

29 Z. L. Wu, M. Moshe, J. Greener, H. Therien-Aubin, Z. Nie, E. Sharon and E. Kumacheva, Three-Dimensional Shape Transformations of Hydrogel Sheets Induced by Small-Scale Modulation of Internal Stresses, *Nat. Commun.*, 2013, **4**, 1586–1587, DOI: 10.1038/ncomms2549.

30 H. Thérien-Aubin, Z. L. Wu, Z. Nie and E. Kumacheva, Multiple Shape Transformations of Composite Hydrogel Sheets, *J. Am. Chem. Soc.*, 2013, **135**(12), 4834–4839, DOI: 10.1021/ja400518c.

31 E. Hajiesmaili and D. R. Clarke, Reconfigurable Shape-Morphing Dielectric Elastomers Using Spatially Varying Electric Fields, *Nat. Commun.*, 2019, **10**(1), 10–16, DOI: 10.1038/s41467-018-08094-w.

32 R. W. Mailen, C. H. Wagner, R. S. Bang, M. Zikry, M. D. Dickey and J. Genzer, Thermo-Mechanical Transformation of Shape Memory Polymers from Initially Flat Discs to Bowls and Saddles, *Smart Mater. Struct.*, 2019, **28**(4), 045011, DOI: 10.1088/1361-665X/ab030a.

33 E. Siéfert, E. Reyssat, J. Bico and B. Roman, Bio-Inspired Pneumatic Shape-Morphing Elastomers, *Nat. Mater.*, 2019, **18**(1), 24–28, DOI: 10.1038/s41563-018-0219-x.

34 A. Laskar, O. E. Shklyaev and A. C. Balazs, Designing Self-Propelled, Chemically Active Sheets: Wrappers, Flappers, and Creepers, *Sci. Adv*, 2018, **4**, 1–12, DOI: 10.1126/sciadv.aav1745.

35 A. Laskar, O. E. Shklyaev and A. C. Balazs, Collaboration and Competition between Active Sheets for Self-Propelled Particles, *Proc. Natl. Acad. Sci. U. S. A.*, 2019, **116**(19), 9257–9262, DOI: 10.1073/pnas.1901235116.

36 S. Das, O. E. Shklyaev, A. Altemose, H. Shum, I. Ortiz-Rivera, L. Valdez, T. E. Mallouk, A. C. Balazs and A. Sen, Harnessing Catalytic Pumps for Directional Delivery of Microparticles in Microchambers, *Nat. Commun.*, 2017, **8**, 1–10, DOI: 10.1038/ncomms14384.

37 O. E. Shklyaev, H. Shum, A. Sen and A. C. Balazs, Harnessing Surface-Bound Enzymatic Reactions to Organize Microcapsules in Solution, *Sci. Adv.*, 2016, **2**(3), e1501835, DOI: 10.1126/sciadv.1501835.

38 S. Lim, A. Ferent, X. S. Wang and C. S. Peskin, Dynamics of a Closed Rod with Twist and Bend in Fluid, *SIAM J. Sci. Comput.*, 2008, **31**(1), 273–302.

39 S. Chandrasekhar, *Hydrodynamic and Hydro Magnetic Stability*, Clarendon Press, Oxford, 1961.

40 C. S. Peskin Downloaded 10/15/15 to 103. 21. 127. 78. Redistribution Subject to SIAM License or Copyright; See Http://Www.Siam.Org/Journals/Ojsa.Php DYNAMICS OF A CLOSED ROD WITH TWIST AND BEND Copyright © by SIAM. Unauthorized Reproduction of This Article I. 2008, **31**(1), 273–302.

41 K. A. Johnson and R. S. Goody, The Original Michaelis Constant: Translation of the 1913 Michaelis-Menten Paper, *Biochemistry*, 2011, **50**(39), 8264–8269, DOI: 10.1021/bi201284u.

42 S. Maiti, O. E. Shklyaev, A. C. Balazs and A. Sen, Self-Organization of Fluids in a Multi-Enzymatic Pump System, *Langmuir*, 2019, **35**, 3724–3732, DOI: 10.1021/acs.langmuir.8b03607.

43 S. Sengupta, D. Patra, I. Ortiz-Rivera, A. Agrawal, S. Shklyaev, K. K. Dey, U. Córdova-Figueroa, T. E. Mallouk and A. Sen, Self-Powered Enzyme Micropumps, *Nat. Chem.*, 2014, **6**(5), 415–422, DOI: 10.1038/nchem.1895.

44 D. R. Nelson, T. Piran and S. Weinberg, *Statistical Mechanics of Membranes and Surfaces*, 2004.

45 A. Oron, S. H. Davis and S. G. Bankoff, Long-Scale Evolution of Thin Liquid Films, *Rev. Mod. Phys.*, 1997, **69**(3), 931–980, DOI: 10.1103/revmodphys.69.931.

46 B. Tavakol, G. Froehlicher, D. P. Holmes and H. A. Stone, Extended Lubrication Theory: Improved Estimates of Flow in Channels with Variable Geometry, *Proc. R. Soc. A*, 2017, **473**(2206), 20170234, DOI: 10.1098/rspa.2017.0234.

47 L. G. Leal, *Laminar Flow and Convective Transport Processes*, Elsevier, 1992, vol. 251.

48 P. Chelikani, I. Fita and P. C. Loewen, Cellular and Molecular Life Sciences Diversity of Structures and Properties among Catalases, *Cell. Mol. Life Sci.*, 2004, **61**, 192–208, DOI: 10.1007/s00018-003-3206-5.

49 G. F. Gaetani, A. M. Ferraris, M. Rolfo, R. Mangerini, S. Arena and H. N. Kirkman, Predominant Role of Catalase in the Disposal of Hydrogen Peroxide within Human Erythrocytes, *Blood*, 1996, **87**(4), 1595–1599.

50 P. Howell, G. Kozyreff and J. Ockendon, *Applied Solid Mechanics*, Cambridge University Press, 2009, vol. 43.